

PHOTONICS Research

From localized to propagating surface plasmon resonances in Au nanoparticle-coated optical fiber sensors and its implications in biosensing

PAULO S. S. DOS SANTOS,^{1,2} JOÃO P. MENDES,¹ JORGE PÉREZ-JUSTE,^{3,4} I. PASTORIZA-SANTOS,^{3,4,*} ID
JOSÉ M. M. DE ALMEIDA,^{1,5} ID AND LUÍS C. C. COELHO¹ ID

¹INESC TEC–Institute of Systems and Computer Engineering, Technology and Science, and Department of Physics, Faculty of Sciences, University of Porto, Rua do Campo Alegre, 4169-007 Porto, Portugal

²Faculty of Engineering, University of Porto, Rua Dr. Roberto Frias, 4200-465 Porto, Portugal

³CINBIO, Universidade de Vigo, Campus Universitario Lagoas, Marcosende, 36310 Vigo, Spain

⁴SERGAS-UVIGO, Galicia Sur Health Research Institute (IIS Galicia Sur), 36312 Vigo, Spain

⁵Department of Physics, School of Science and Technology, University of Trás-os-Montes e Alto Douro, 5001-801 Vila Real, Portugal

*Corresponding author: pastoriga@uvigo.gal

Received 11 January 2024; revised 20 May 2024; accepted 8 July 2024; posted 9 July 2024 (Doc. ID 518181); published 16 September 2024

Nanoparticle-based plasmonic optical fiber sensors can exhibit high sensing performance, in terms of refractive index sensitivities (RISs). However, a comprehensive understanding of the factors governing the RIS in this type of sensor remains limited, with existing reports often overlooking the presence of surface plasmon resonance (SPR) phenomena in nanoparticle (NP) assemblies and attributing high RIS to plasmonic coupling or waveguiding effects. Herein, using plasmonic optical fiber sensors based on spherical Au nanoparticles, we investigate the basis of their enhanced RIS, both experimentally and theoretically. The bulk behavior of assembled Au NPs on the optical fiber was investigated using an effective medium approximation (EMA), specifically the gradient effective medium approximation (GEMA). Our findings demonstrate that the Au-coated optical fibers can support the localized surface plasmon resonance (LSPR) as well as SPR in particular scenarios. Interestingly, we found that the nanoparticle sizes and surface coverage dictate which effect takes precedence in determining the RIS of the fiber. Experimental data, in line with numerical simulations, revealed that increasing the Au NP diameter from 20 to 90 nm (15% surface coverage) led to an RIS increase from 135 to 6998 nm/RIU due to a transition from LSPR to SPR behavior. Likewise, increasing the surface coverage of the fiber from 9% to 15% with 90 nm Au nanoparticles resulted in an increase in RIS from 1297 (LSPR) to 6998 nm/RIU (SPR). Hence, we ascribe the exceptional performance of these plasmonic optical fibers primary to SPR effects, as evidenced by the nonlinear RIS behavior. The outstanding RIS of these plasmonic optical fibers was further demonstrated in the detection of thrombin protein, achieving very low limits of detection. These findings support broader applications of high-performance NP-based plasmonic optical fiber sensors in areas such as biomedical diagnostics, environmental monitoring, and chemical analysis. © 2024 Chinese Laser Press

<https://doi.org/10.1364/PRJ.518181>

1. INTRODUCTION

The development of advanced sensing technologies has become an indispensable tool for various applications, ranging from environmental monitoring to biomedical diagnostics [1–4]. Among these cutting-edge technologies, plasmonic optical fiber sensors have emerged as a promising avenue due to their ability to harness the unique optical properties of both nanoparticles (NPs) and optical fibers [5–8]. By leveraging the exceptional light-matter interactions that occur at the nanoscale, plasmonic optical fiber sensors can offer unprecedented sensitivity and selectivity, making them ideal candidates for ultrasensitive detection and real-time monitoring [9–15].

Specifically, using an optical fiber with immobilized plasmonic NPs at the core surface, each particle exhibits localized surface plasmon resonance (LSPR), intensifying the electromagnetic fields at their surfaces [16]. Besides the LSPR modes can also engage in intricate interactions with each other and even with the substrate, giving rise to interesting collective or hybrid plasmonic effects [17–19]. These depend on NP size, shape, and arrangement as well as NP-substrate and NP-NP spacing [20–24]. Since these parameters collectively determine the ultimate sensitivity to refractive index (RI) changes in the surrounding medium, understanding the interplay between these factors is crucial for tailoring the sensor response and

optimizing its performance. Plasmonic coupling of densely packed NPs can be observed mainly through the LSPR shift due to neighboring NP interaction and is primarily dependent on interparticle spacing [17,25,26]. Thus, at small interparticle distances, highly intense electromagnetic fields (hot spots) are generated, which can prove beneficial for sensing applications like surface-enhanced Raman scattering (SERS) or light-matter interaction enhancement [27–29]. Interestingly, 1D or 2D NP arrays can also give rise to collective plasmonic modes that interact and propagate throughout the entire NP array showing similar behavior to the surface plasmon resonance (SPR) observed in plasmonic thin films [30,31].

Nevertheless, the considerable variability in the refractive index sensitivity (RIS) observed for NP based plasmonic optical fiber sensors may suggest another plasmonic mechanism. For example, focusing solely on studies involving Au nanospheres, whilst Mie theory predicts RIS between 30 and 80 nm per refractive index unit (RIU), the RIS values reported for Au NPs deposited on optical fibers range from 50 to 2016 nm/RIU [16,32–41]. These wide range RIS values also contrast with the low RIS values obtained experimentally from colloidal dispersions and NPs immobilized on flat glass substrates [13,36,42–44]. Despite extensive investigations, the prevailing explanations for these behaviors mainly attribute the observed sensitivities to either: (1) the formation of hot spots among NPs due to interparticle coupling; (2) the light-waveguiding mechanisms observed in insulator-metal-insulator (IMI) like structures as continuous metal films or ordered NPs arrays [35,45–47]; (3) the excitation of lossy mode resonances (LMRs) in the polyelectrolytes layer (PEL) [40,48,49]. However, it has become evident that the first explanation alone fails to account for the high sensitivities reported, as perfectly aligned and spaced dimers and trimers are only capable of presenting a maximum RIS of around 500 nm/RIU [50]. Regarding the light-waveguiding mechanisms, Otte *et al.* [35] proposed this mechanism considering the IMI structure composed by a metal layer of sparse Au nanoellipsoids of high aspect ratios (modeled by a homogeneous and anisotropic effective RI layer) located between a glass substrate and the external medium. Later, Spacková *et al.* presented similar results [51]. Regardless of the reported high RIS values, the capability to obtain the required highly effective RI layer with lower aspect-ratio NPs was not demonstrated. Also, the proposed numerical model should create an evanescent field towards the external medium (like the SPR wave obtained through plasmonic thin films). Finally, as the study was conducted on planar substrates, the optical behavior obtained on optical fiber platforms with randomly immobilized NPs is yet to be studied. Finally, regarding the LMR effect, a thick PEL is required to observe the effect of the RIS being dependent on PEL thickness when above the NPs. Nevertheless, no LMR effect is produced when a thin PEL is between the fiber and the NPs [40].

The numerical modeling of sensors based on optical fibers coated with plasmonic NPs from the aforementioned authors can also provide great insights into the underlying physical mechanisms. These range from simpler studies based on Mie scattering for plasmonic NPs in solution to NPs affected by retardation effects on their polarizability due to the presence

of a substrate, interparticle coupling effects by changing their mean distance, or even approaches using an effective medium approximation provided by Maxwell Garnett theory [52–54]. The latter is of special relevance in the simulations of immobilized NPs over waveguiding structures, such as optical fibers, as interesting coupling phenomena can arise from the interaction with guided light [55,56].

Herein, we carry out theoretical and experimental investigations into the phenomena (LSPR and/or SPR) that determine the sensitivity of randomly assembled Au nanoparticle optical fibers to changes in refractive index. Thus, we deeply analyze the effect of the NP size and NP surface coverage in the optical response of the fiber to determine the optimal conditions for enhanced RIS. Besides, experimental results are compared to numerical outcomes from discretization of many interacting NPs or by treating them as a homogeneous plasmonic layer. Finally, the efficacy of the plasmonic sensing configuration will be validated for the purpose of biological sensing, specifically for the detection of thrombin protein (THR). This protein is a serine protease which regulates hemostasis and blood coagulation. Thus, fast and precise measurements can help to assess individual needs and mitigate possible clinical conditions. In this study, THR binding aptamers will be used as they assure the best measurement specificity [57–61].

2. RESULTS AND DISCUSSION

A. Experimental Setup and Numerical Modeling

The sensor configuration is based on an optical fiber sensor tip, which includes a decladded section with immobilized gold NPs (Fig. 1). Additionally, a silver film is deposited onto the end

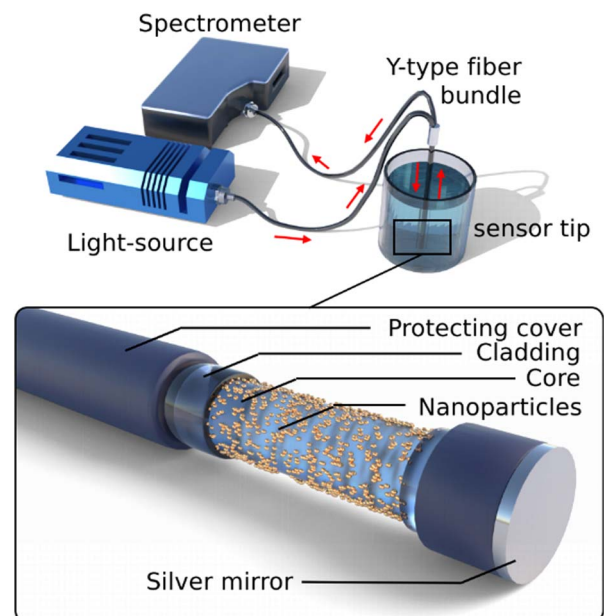


Fig. 1. Optical fiber sensing scheme composed of a broadband light source and a spectrometer to measure the plasmonic NP response on the fiber optic sensing probe. This probe is based on a 1 cm core-exposed section near the optical fiber cleaved tip (onto which a silver mirror was previously deposited).

facet of the fiber, forming a mirror. This design allows for interaction between the evanescent field and Au NPs while enabling real-time monitoring of the Au NP deposition on the decladded section.

The bulk behavior of assembled Au NPs on the optical fiber was investigated using an effective index medium approximation (EMA), such as the gradient effective medium approximation (GEMA) proposed by Czajkowski *et al.* [62]. In this scenario, instead of discretizing a large number of NPs (computationally intensive), the system is approximated by a homogeneous layer of a given RI [52]. This approximation provides a more accurate model compared to the widely used Maxwell

method can be calculated as follows. First, a layer stack with a partial density (f_{partial}) equivalent to the discretized section along the NP height is given by Eq. (1):

$$f_{\text{partial}} = \frac{6hL(1+L)R - 3b^2L^2 - 2(2+3L)R^2}{2R^2L^3}, \quad (1)$$

where R is the NP radius, L is the number of discretized layers, and h is the layer height. The effective layer density (f_{layer}) is then obtained by multiplying the calculated f_{partial} by the total NP density (f_{NP}). Finally, the effective index of each layer e_{eff}^i is calculated as follows using a modified MG theory for accounting for both NP anisotropy and size [63]:

$$\epsilon_{\text{eff}}^i = \epsilon_m \frac{\epsilon_m + (L_i(1 - f_{\text{layer}}) + f_{\text{layer}})(\epsilon_{\text{NP}} - \epsilon_m) + (\epsilon_m - \epsilon_{\text{NP}})(1 - f_{\text{layer}})\Delta}{\epsilon_m + L_i(1 - f_{\text{layer}})(\epsilon_{\text{NP}} - \epsilon_m) + (\epsilon_m - \epsilon_{\text{NP}})(1 - f_{\text{layer}})\Delta}, \quad (2)$$

Garnett (MG) or Bruggeman models, which are extensively employed for accurately describing the behavior of plasmonic NPs [52,63]. This enhanced accuracy is attributed to the fact that the NPs are not simply described by a single homogeneous layer but involve multiple layers. Besides, this method allows geometrical anisotropies to be taken into account and the overall improvement of geometry accuracy by creating a gradient-like layer stack. Figure 2A shows the simulation model using a transfer-matrix method (TMM) formalism with a light cone incident from the fiber core, corresponding to the multimodal behavior on a paraxial approximation and a detection layer in the same layer. The effective index of each layer for this GEMA

where ϵ_m and ϵ_{NP} are the permittivity of the surrounding medium and NP, respectively. $\Delta = x^2 + 2/3ix^2$, where x is a size parameter given by $x = \pi R \sqrt{\epsilon_m}/\lambda$. Finally, L_i is the geometrical factor for the ellipsoidal NP, which is 1/3 for Au nanospheres.

Interestingly, increasing the Au density on the effective layer, a wavelength red-shift can be observed in both the real and imaginary components of their effective index (see Appendix B, Fig. 8). Finally, by varying the same NP density, a steep increase in the effective index profile on the NP region as can be observed in Fig. 2B for a 50 nm Au NP.

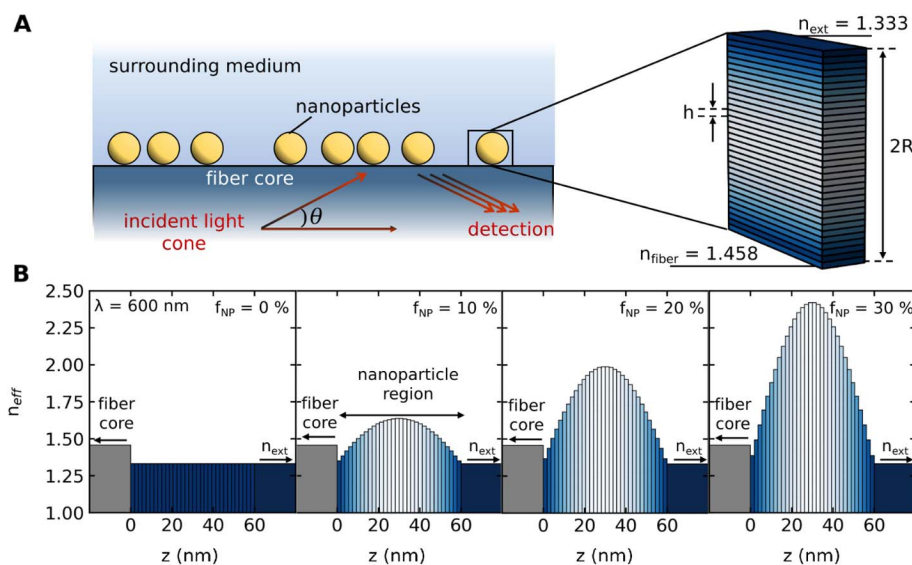


Fig. 2. A: Schematic representation of the simulation setup where the random ensemble of Au NPs immobilized over the fiber core was approximated by a gradient effective index method (GEMA). This method divides the NPs into multiple homogeneous layers with an effective RI given by Maxwell-Garnett theory. B: Real component of the effective index profile for the multiple GEMA layers at several NP coverage densities for 50 nm NPs.

B. Plasmonic Properties of Au Nanoparticle-Coated Optical Fiber

The deposition of Au NPs with sizes 20, 50, and 90 nm was carried out via electrostatic interactions employing the layer-by-layer (LbL) approach [25]. Thus, citrate-stabilized Au NPs of 50 nm with negative charge were uniformly deposited via immersion on the positively charged optical fiber (see experimental part for further details). Figure 3A shows the kinetics of 50 nm Au NP deposition, and Fig. 3C shows the SEM images of the Au NPs uniformly deposited at different immersion times, as indicated. The initial stages of Au NP immobilization (Fig. 3A) clearly show a single band increasing in intensity at 550 nm, corresponding to the LSPR band of individual Au NPs. However, as the NP density on the fiber surface (f_{NP}) increases, interparticle coupling effects start causing an LSPR red-shift (Fig. 3B). After 15 min, a second band appears at longer wavelengths due to collective plasmonic effects with a faster growth rate than the LSPR band [see scanning electron microscope (SEM) images in Fig. 3C]. At a later stage, around

30 min, it is visible that the LSPR band ceased growing and red-shifting, while the other continued to grow and red-shift at a higher rate and without significant band widening (Figs. 3A and 3B). This finding establishes that the rightmost band does not arise from interparticle coupling, but rather from an alternative collective plasmonic mechanism mainly reliant on particle density.

Further verification of the physical driving mechanisms underlying both peaks was achieved through two numerical methods: a scattering-matrix method and GEMA model with the TMM algorithm. The first method was used for the calculation of the electromagnetic fields of the Au NPs deposited on the fiber. In the model, hundreds of 50 nm Au NPs were discretized and randomly distributed on top of a glass layer (total area of $1 \mu\text{m}^2$) and immersed in a constant dielectric medium ($n = 1.333$). The total number of NPs was varied according to the desired NP density. Then, light-particle interaction was accomplished from the evanescent field coming through the glass layer. As shown in Fig. 3D, a total particle population density

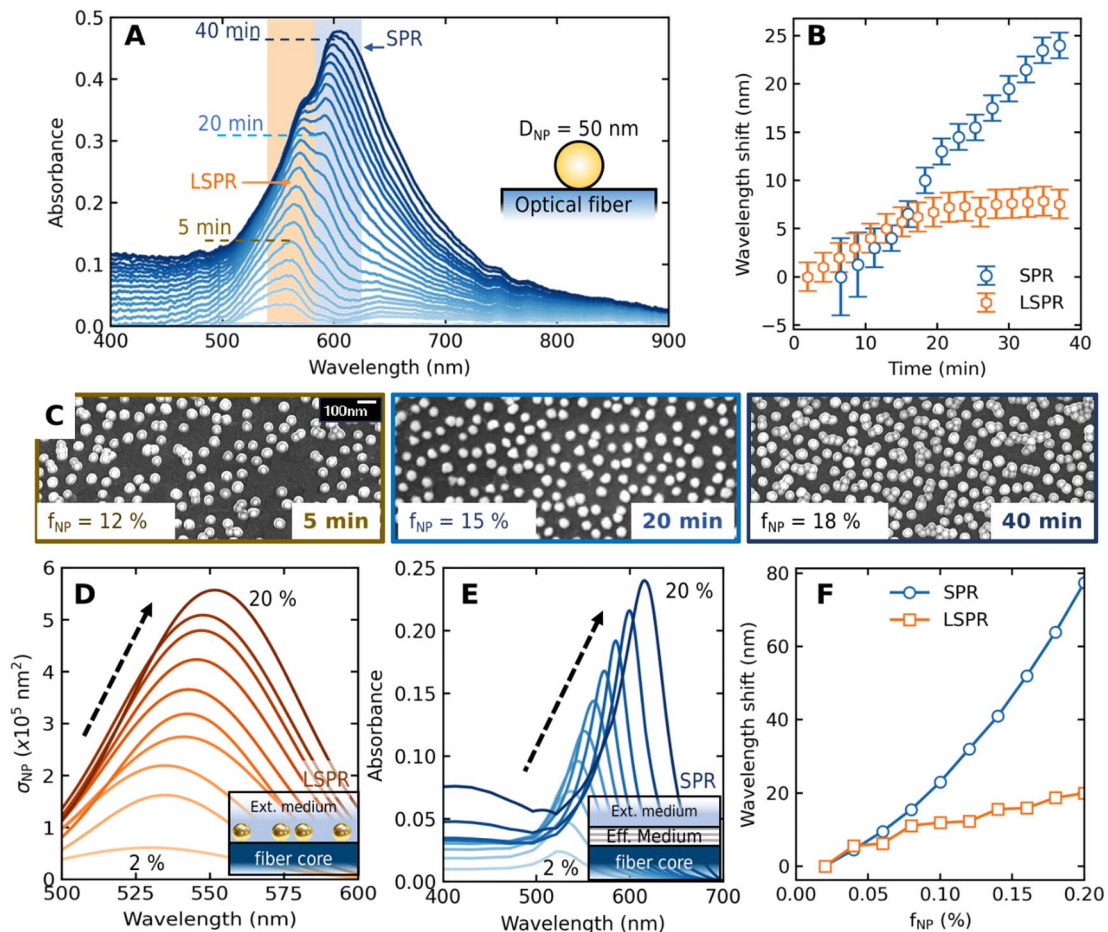


Fig. 3. A: Au NP deposition kinetics onto the optical fiber sensor, showing two plasmonic bands dependent on the deposition time. The Au NP diameter is 50 nm. B: Time evolution of the wavelength shift of both plasmonic modes during 50 nm Au NP immobilization. C: Scanning electron microscope (SEM) images of the Au NPs on optical fibers at different deposition times (5, 20, and 40 min). The estimated value of NP densities on the fiber surface (f_{NP}) is included. D: Extinction cross section of Au NPs deposited on fiber for different NP densities (from 2% to 20%) calculated using a scattering-matrix formalism. As a model, hundreds of discretized Au NPs randomly positioned on $1 \mu\text{m}^2$ were employed. E: Calculated absorbance for different Au densities (from 2% to 20%) obtained via TMM using the GEMA. A strong correlation between the red-shifts and absorbance increases of the plasmonic band with NP density. F: Comparison on wavelength shifts as a function of the NP fiber surface coverage calculated through a scattering-matrix formalism and TMM.

augmentation from 2% to 20% caused an intensity increase accompanied by 20 nm red-shift. Such behavior can be undoubtedly attributed to increased interparticle coupling. On the other hand, simulations involving the GEMA model with the TMM algorithm were conducted with a 50 nm total stack layer height and subdivided into 20 layers. The effective layer's parameters were also calculated for different NP densities. The results indicate accordance with the experimental findings, showing a strong correlation between larger red-shifts and increased NP density (Fig. 3E). Furthermore, the density-induced increase in wavelength shift exhibits greater prominence in this plasmonic mode compared to modified LSPR resulting from interparticle coupling (Fig. 3F), aligning with experimental observations. This plasmonic phenomenon is likely linked to SPR excitation obtained in plasmonic thin-film devices, and the increase in NP density serves the purpose of modulating the meta-layer effective RI. Such an approximation is valid due to the much smaller size when compared to the light wavelength. The linking to SPR phenomena is also indicated by the GEMA structure response under p- or s-polarizations (see Appendix B, Fig. 9). Under s-polarization an increase of f_{NP} results in the intensity increase of the LSPR band without a significant wavelength shift towards longer wavelengths, whereas under p-polarized light, the structure shows a strong shift to longer wavelengths. The sum

of both polarizations shows a similar response as observed experimentally.

A deeper insight into the nature of the plasmonic phenomena can be achieved through the calculation of the dispersion curves for the sensor configuration, as dispersion curves are visual representations of how the material RI changes with the light wavelength. As shown in Fig. 4A, the light dispersion curves on the NP meta-layer obtained as a function of f_{NP} evidence strong light dispersion as typically observed on SPR. Also, the dispersion curves cross the fiber light cone at successively longer wavelengths with increased f_{NP} , which agrees with the observed wavelength red-shifts during the particle's immobilization (Fig. 3A). The field distribution can also provide useful insights into the underlying mechanism behind the observed optical response. The existence of an SPR phenomenon is further backed by the electric field spatial distribution (Fig. 4B). This field shows the typical sinusoidal intensity profile inside the fiber, accompanied by a strong field enhancement in the metal/external interface and an exponential decay towards the external medium. Thus, no light waveguiding mechanism was observed, which should be characterized by a strong field locality in the center of the meta-layer. Moreover, this field profile is also highly dependent on f_{NP} since the field enhancement increases with f_{NP} . The larger field on the outside region also increases the band dependency on

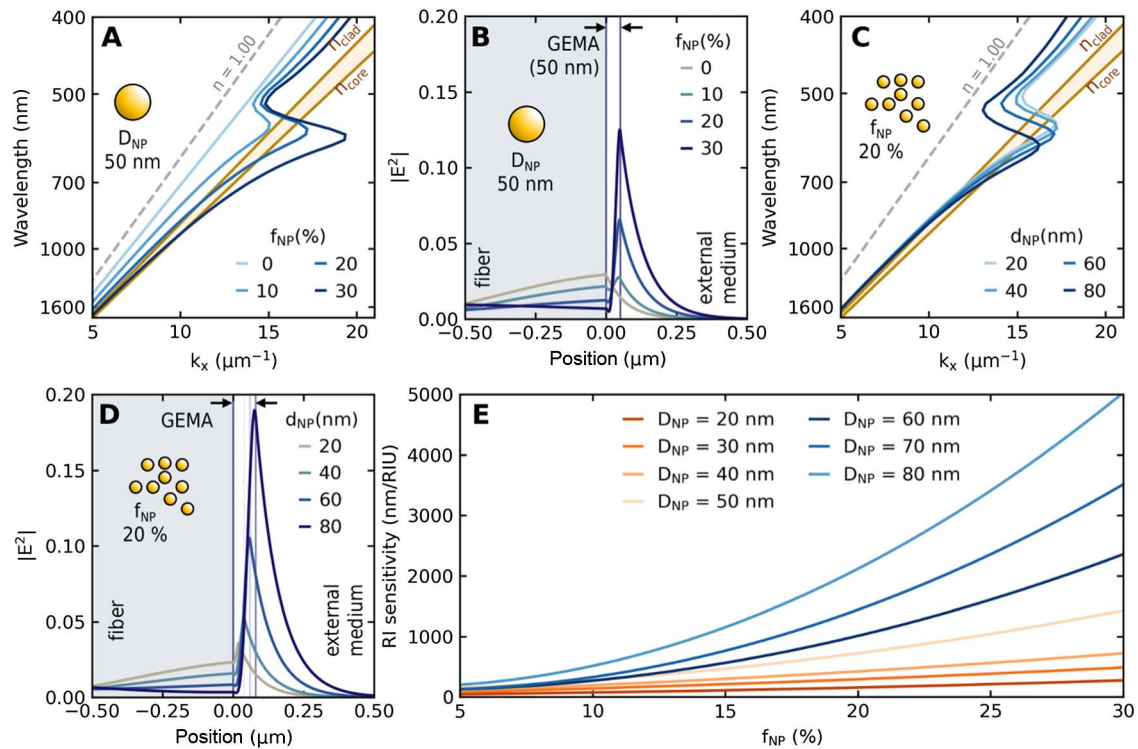


Fig. 4. A: Calculated dispersion curves for a 50 nm effective index plasmonic layer on the fiber surface at various NP densities (f_{NP}), ranging from 0 to 30%. The dispersion curves intersect with the fiber light cone at wavelengths from 720 to 950 nm depending on f_{NP} . The dotted line represents the wavevector of light in vacuum. B: E-field spatial distribution for 50 nm NPs using the GEMA with different f_{NP} , showing a steep increase towards the metal layer and long decay towards the external medium. C: Dispersion curves for several NP sizes at a constant f_{NP} of 20%, causing the intersection with the fiber light cone at successively larger wavelengths. D: Field distribution within the GEMA method with a constant f_{NP} of 20% for different NP diameters as indicated, showing stronger E-fields for larger NPs. E: Refractive index sensitivity for optical fibers with different NP densities. NP diameters range between 20 and 80 nm. The values were measured around 1.340.

the surrounding RI, a feature highly desirable for optimizing plasmonic sensor construction.

When studying the effect of the NP size, we found that the dispersion curves of the plasmonic meta-layer were dependent on its dimensions (consequently on the NP diameter), intersecting the fiber light cone at successively longer wavelengths for larger NPs (Fig. 4C). Finally, the NP size increase is also related to stronger fields on the surrounding medium (Fig. 4D). Therefore, higher NP densities and sizes should promote higher sensitivities, as numerically observed (Fig. 4E).

C. Effect of Nanoparticle Size and Density on Refractive Index Sensitivity

Next, we experimentally investigated the effect of f_{NP} on the RI sensitivity of the optical fiber. Therefore, optical fibers with immobilized 51 nm Au NPs at f_{NP} ranging from 18% to 22% were analyzed by immersing them in solvents with different RIs. The plot of the wavelength as a function of solvent RI shows a nonlinear behavior (Fig. 5A). The curves also indicated a higher RIS for larger f_{NP} . Indeed, if we estimate the RIS in the vicinity of 1.34, values from 310 to 580 nm/RIU are obtained. Finally, larger values from 1698 to 3354 nm/RIU are obtained in the RI range near 1.41.

Interestingly, the nonlinear behavior on RIS regardless of f_{NP} is typical of SPR as previously reported [9,64–67]. It is simply due to the phase-matching conditions that need to occur and are dependent on a complex relation between the plasmonic material and external medium permittivity, as given by [68]

$$k_{SP} = \frac{2\pi}{\lambda} \sqrt{\frac{\epsilon_{metal}\epsilon_{medium}}{\epsilon_{metal} + \epsilon_{medium}}}, \quad (3)$$

where k_{SP} is the light wavevector, λ is the light wavelength, and ϵ_{metal} and ϵ_{medium} are the metal and the external medium permittivity, respectively.

Notably, despite the larger particle size ($D = 87$ nm) and lower particle density in comparison to the smaller NPs, significantly higher RI sensitivities were achieved (Fig. 5B). The analysis of smaller NPs (21 nm) presented in Fig. 5C revealed the smallest RIS enhancement, in line with the numerical results of Fig. 4E. The observed RIS for an f_{NP} of 16% is nearly ten times smaller than that observed with only an f_{NP} of 9% for the 87 nm NP-coated fiber, highlighting the relevance of the NP size for this effect. Moreover, by tracing a vertical line at a constant f_{NP} , e.g., 20%, in Fig. 4E, it can be seen that a linear increase in the NP diameter results in a nonlinear RIS enhancement. This aspect is highlighted in Appendix B (Fig. 10), where the RI sensitivity is analyzed. Thus, for a given f_{NP} , the NP size is the most determinant factor impacting the observed ΔRIS between f_{NP} values of 10% and 20% at different NP diameters. Also, representative SEM images of the different Au NP sizes and densities are shown in Fig. 5D, thus evidencing a uniform NP deposition. The analysis of the RIS for the different samples (solid lines in Fig. 5C) unveils a strong correlation between the NP diameter and the initial red-shift and RI sensitivity. Moreover, the GEMA based simulations (dashed lines in Fig. 5C) are in good agreement with the experimental results.

Another interesting effect can be observed by experimentally changing the surrounding medium from water ($n = 1.333$) to air ($n = 1.000$), causing the SPR band to disappear and the reappearance of the LSPR band (Fig. 6A). The same effect can be observed in the calculated dispersion curves when the RI changes from 1.333 to 1.000 (Fig. 6B). The most

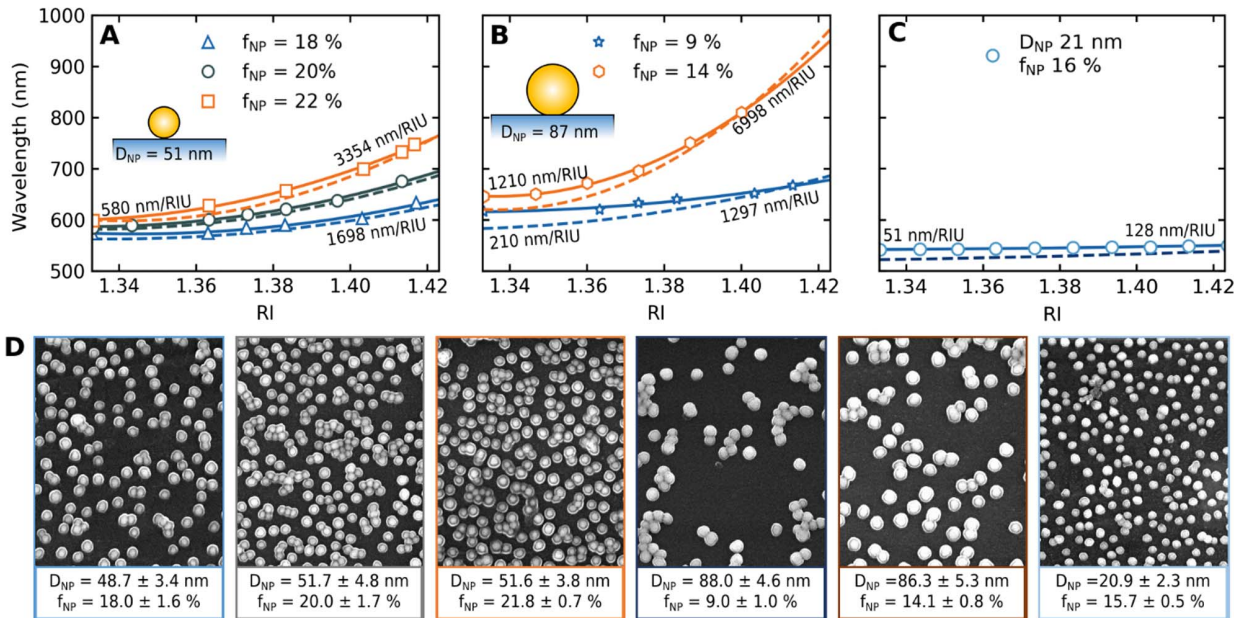


Fig. 5. A: Refractive index sensitivity of optical fibers immobilized with 51 nm Au NPs with f_{NP} of 18%, 20%, and 22%, as indicated. B: Refractive index sensitivity of optical fibers immobilized with 87 nm Au NPs with f_{NP} of 9% and 14%. C: Refractive index sensitivity of optical fibers immobilized with 21 nm Au NPs with f_{NP} of 16%. The white filled markers correspond to experimental data, while the solid curves represent a second-order polynomial fitting curve. Dashed curves are the numerical results obtained through the GEMA method. D: Representative SEM images of optical fibers with immobilized Au NPs of different sizes (D_{NP}). The NP density on the fiber surface (f_{NP}) is also indicated.

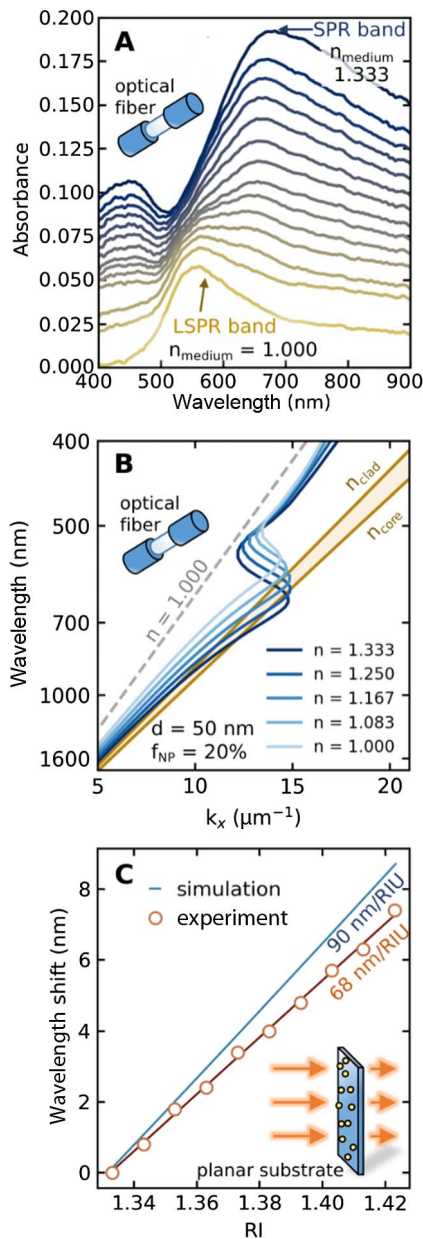


Fig. 6. A: Experimental optical properties recorded with a 50 nm Au NP immobilized optical fiber immobilized upon changing the refractive index of the surrounding medium from water ($n = 1.333$) to air ($n = 1.000$). B: Dispersion curves of the Au meta-layer calculated for different refractive indexes (ranging from 1.333 to 1.000) via the GEMA method. C: Comparison between the experimental and numerical results on RIS of 50 nm Au NPs immobilized on a planar glass substrate under perpendicular illumination. The numerical results were obtained through the scattering-matrix method formalism for an NP density of 15%.

important aspect lies with the absence of any intersection between the fiber light cone and the meta-layer dispersion curve, showing that with a surrounding medium with $n = 1.000$, it is impossible to excite the SPR. Additional experiments were performed on planar substrates featuring immobilized Au NPs of different sizes, employing the same immobilization process and conditions as used with the optical fibers. As shown in Fig. 6C,

the wavelength shift exhibits a linear relationship with the solvent RI being the estimated RIS of 68 nm/RIU. These findings unequivocally indicate that the excitation of the SPR under perpendicular incident illumination is not possible.

D. Thrombin Detection

Impelled by the enhanced RIS observed on denser and larger NP ensembles, the potential of Au NP immobilized optical fiber for biosensing applications was investigated. To validate its performance, the detection of thrombin protein (THR) was chosen as the model system. Since THR plays an important role in the blood coagulation cascade and homeostasis, its typical values found in a healthy adult human depend on numerous factors. However, the traditional metric to quantify the THR level kinetics is the time to achieve a 2 nM (1 nM = 1 nmol/L) level, usually referred to as the “clot time,” which is often reached in less than 5 min [69]. The typical maximum THR concentration in a healthy individual is about 100 nM. Therefore, a test range with THR concentrations from 0.01 to 100 nM was performed.

Initially, two fibers were coated with 70 nm Au NPs (f_{NP} 7% and 14%). The RISs of both fibers were measured to be of 544 and 1301 nm/RIU (measured at an external RI around 1.340) for f_{NP} of 7% and 14%, respectively. At a higher surrounding RI, around 1.39, their RIS increased considerably, reaching 1110 and 2385 for f_{NP} of 7% and 14%, respectively (see Figs. 7A and 7B). For the thrombin detection, the Au NP immobilized optical fibers were first functionalized with a poly-L-lysine (PLL) layer and after that with thrombin binding aptamers (TBAs), resulting in a red-shift of the main band due to the increased RI around the NPs (Fig. 7C). The fiber sensors were first sequentially exposed to increasing concentrations of THR (30 min of incubation time, see experimental section for further details). The optical properties were recorded at the final stage of each incubation step on the Tris buffer solution, which was also used as the washing solution. As shown in Fig. 7D, a red-shift was observed with higher concentrations of THR, although more pronounced for the higher NP density sensor. The experimental data followed a sigmoid-shaped profile and were fitted using the Hill model since it has been demonstrated as the best model for the aptamer–thrombin interaction [70]:

$$y = \lambda_{\text{max}} \frac{x^n}{k^n + x^n}, \quad (4)$$

where x and y are the THR concentration and sensor response, respectively. λ_{max} is the maximum wavelength shift [71]. Note that the Hill equation returns k as a metric of binding, and n , the Hill coefficient. k represents the concentration of protein at half-maximal binding, and n reports on cooperativity. The best fit to the experimental data with Eq. (4) yielded the curve in Fig. 6B and the following values for the parameters: $k = 2.42 \pm 0.10$ nM and 59.59 ± 754.0 nM, and $n = 0.94 \pm 0.14$ and 0.33 ± 0.01 for the 7% and 14% concentration configurations, respectively. The value of k is essentially undetermined in both cases due to the relatively high detection range of the sensor, at least four orders of magnitude. Interestingly, the uncertainty for the 14% concentration configuration suggests a higher detection range. On the other hand, n values smaller than 1 indicate the occurrence of a negatively cooperative

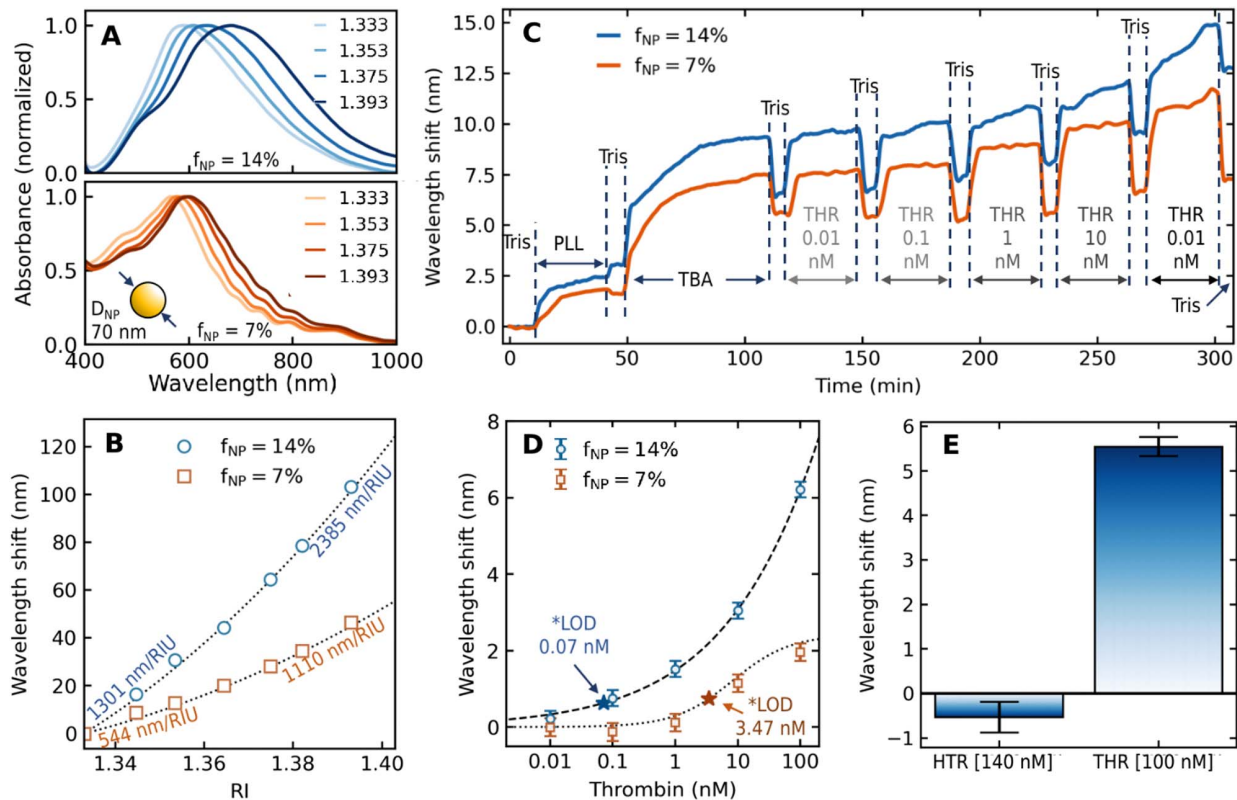


Fig. 7. Experimental results obtained for optical fibers coated with 70 nm Au NPs at f_{NP} of 7% and 14%: absorption spectra (A) and RIS comparison (B). C: Real-time tracking of the plasmonic band of two Au NP immobilized optical fibers during the functionalization with PLL and TBA, as well as the THR binding events with TBA. The diameter of Au NPs was 70 nm and f_{NP} was 7% and 14%, as indicated. D: Wavelength shift as a function of THR concentration, as measured at the final of each incubation period (in the Tris solution), for both optical fibers covered with NP at a total f_{NP} of 7% and 14%. The dashed curves represent the Hill fitting of the experimental data. LODs are indicated. E: Cross-sensitivity test with HTR showing negligible interference for the optical fiber sensor configurations covered with an f_{NP} of 14%.

binding, which is an expected behavior since the probability of binding reduces as the surface covering increases. The estimated limit of detection (LOD) determined as the concentration of antigen that generates 10% of the signal of the control samples (EC10) is 0.07 and 3.47 nM for the 7% and 14% concentration configurations, respectively. The LOD is displayed explicitly by a star marker in Fig. 7D. The near 50-fold decrease in the obtained LOD underlines the significance of the NP density increase, and an LOD well below the 2 nM level of the “clot time” ensures great resolution to THR efficient detection. These results are better than comparative studies with plasmonic optical fiber-based sensors that show LOD between 0.54 and 100 nM [57–59,61].

Finally, to evaluate cross-sensitivity, the sensor was incubated with human transferrin (HTR) protein (140 nM). The analysis of the optical response did not reveal a wavelength red-shift (Fig. 7E) indicating negligible HTR binding.

3. CONCLUSION

In summary, we have theoretically demonstrated that randomly immobilized Au NP-coated optical fibers can support SPR. Moreover, we established a clear distinction between the LSPR and SPR supported by these plasmonic optical fibers. Through the comparison of experimental results with

numerical simulations, we elucidated the complex interplay between LSPR and coupled SPR effects in the plasmonic optical fibers. Thus, larger f_{NP} and NP sizes favor the SPR effect over LSPR. This behavior is not restricted to Au NPs and can be expanded to any plasmonic NPs, regardless of the shape and nature, randomly immobilized on an optical fiber.

Furthermore, studying the effect of Au NP size and surface coverage enabled us to identify the optimal conditions for achieving enhanced RIS and therefore sensing capabilities. Notably, we observed improved sensitivities for optical fiber modified with larger NP size and higher f_{NP} , primarily attributed to the dominating influence of the SPR effect. The experimental RIS of Au NP-based optical fibers with f_{NP} of 15% varied from 135 to 6998 nm/RIU (RI region around 1.39) for an Au NP diameter from 20 to 90 nm. Similarly, 90 nm Au NP-based optical fibers showed RIS from 1297 to 6998 nm/RIU (RI region around 1.39) for f_{NP} between 9% and 14%. These findings offer valuable insights into the design and optimization of plasmonic optical fiber sensing platforms.

Finally, we demonstrated the practical utility of the Au NP-coated optical fibers by detecting THR. Using a 70 nm Au NP-based optical fiber with an f_{NP} of 14%, we achieved a remarkably low LOD of 0.07 nM. This value represents a remarkable improvement compared to those reported in the literature for plasmonic optical fiber-based sensors.

The knowledge gained from this study propels the progress of plasmonic optical fiber sensing, thereby expanding its potential applications across various fields, from biomedical diagnostics to environmental monitoring, and chemical analysis.

APPENDIX A: METHODS

Chemicals. Hydrogen tetrachloroaurate(III) trihydrate ($\text{HAuCl}_4 \cdot 3\text{H}_2\text{O}$), trisodium citrate ($\text{Na}_3\text{C}_6\text{H}_5\text{O}_7$), tannic acid ($\text{C}_{76}\text{H}_{52}\text{O}_{46}$), silver nitrate (AgNO_3), polyethylenimine [PEI, 750 KDa; $\text{H}(\text{NHCH}_2\text{CH}_2)_n\text{NH}_2$], poly-sodium 4-styrenesulfonate [PSS, 70 KDa; $(\text{C}_8\text{H}_7\text{NaO}_3\text{S})_n$], poly-L-lysine [PLL, 0.1% (mass-to-volume ratio) in H_2O], glycerol [$\text{HOCH}_2\text{CH}(\text{OH})\text{CH}_2\text{OH}$], SSPE buffer solution (20× concentrate), Tris base [$\text{H}_2\text{NC}(\text{CH}_2\text{OH})_3$; for molecular biology, 99.9%], potassium hydroxide (KOH), glucose ($\text{C}_6\text{H}_{12}\text{O}_6$), potassium chloride (KCl; Bioextra, 99%), sodium chloride (NaCl; Reagent Plus, 99%), magnesium chloride (MgCl_2 ; anhydrous, 98%), phosphate buffered saline tablets (PBS) α -thrombin from human plasma (THR; lyophilized powder, >2800 NIH units/mg protein), and amine-modified thrombin binding aptamer ($\text{H}_2\text{N-TBA}$; reverse phase HPLC purification) were used for the biosensing assays. Transferrin from human blood plasma (HTR; $\geq 95\%$) was used for cross-reactivity tests. All the used chemicals were purchased from Sigma-Aldrich (Merck Group), except for the Tris base and the $\text{H}_2\text{N-TBA}$, which were purchased from Fisher Scientific (Thermo Fisher Scientific Group) and Eurogentec, respectively. Moreover, all the chemicals were used without additional purification. Ultrapure water (analytical grade), ethanol (EtOH; 96%), and acetone were also used. All glassware was successively cleaned with acetone and ethanol and finally rinsed with Milli-Q water and stored at 60°C before use.

Au nanoparticle synthesis. Citrate-stabilized colloidal Au NPs were synthesized via a seed growth method as previously reported [72]. Thus, Au NPs of 20, 50, 70, and 90 nm in diameter were synthesized. After synthesis, the particles were centrifuged and redispersed in Milli-Q water at one-fifth the initial volume and used as is. The final Au concentration was around 125 mM, as measured by placing the NP solution inside a spectrometer and the absorbance at 400 nm was measured inside a 1 mm glass cuvette.

Optical fiber preparation. A 10 cm portion of a silica core multimode fiber (MMF-FT600UMT, Thorlabs, Dortmund, Germany) with a core/cladding diameter of 600/630 μm was cleaved and both ends polished sequentially with 8 and 3 μm polishing disks (Fibermet, Buehler, Lake Bluff, IL, USA). After mechanically removing a 1 cm portion of the cladding with a fitting stripping tool, the fiber was thoroughly rinsed and then washed in an ultrasonic bath for 10 min. On one end of the fiber, a silver mirror was fabricated with the reduction of silver nitrate by glucose on a potassium hydroxide solution [66].

After rinsing the decladded section with Milli-Q water, the fiber was fixed on a groove of a Teflon platform, and the sensing region was immersed into an aqueous solution of PEI (1 mg/mL, containing 0.5 M NaCl) for 30 min. After three washing steps via immersion in water for 1 min, the optical fiber was immersed in an aqueous solution of PSS (1 mg/mL,

containing 0.5 M NaCl) for 20 min, followed by the same washing procedure. The previous steps were repeated until the formation of a third PEI layer was achieved. Then, the different citrate-stabilized Au NPs were immobilized onto the fiber by immersion of the decladded section into the Au NP dispersions. This step was monitored in real time by connecting the sensing region to a Y-bundle with one end connected to a light source (LS-W, SarSpec, Porto, Portugal) and the other to a spectrometer (Speed+, SarSpec, Porto, Portugal).

Bulk RIS analysis. For the tests for bulk RI sensitivity, different water/glycerol mixtures were prepared in order to have RI values between 1.333 and 1.415. After each measurement, the sensing region was washed three times with pure water (1 min immersion).

Thrombin sensing. Regarding the biosensing evaluation, the sensing region was first washed three times via 1 min immersion with a cleaning buffer solution (Tris). This solution contains 1.2 g of Tris-base, 7.5 g of KCl, and a dropwise addition of HCl 1 M to adjust the solution pH to 7.4 for a final volume of 1 L. The same cleaning procedure was repeated after each incubation and immobilization procedure. Then, citrate-stabilized Au NP immobilized optical fiber was functionalized with TBA as previously reported [58]. Briefly, the Au NP immobilized optical fiber was modified with PLL by immersing the sensing region in an aqueous PLL solution (0.1%, mass-to-volume ratio) for 30 min and then washed with the Tris solution by immersion for 5 min. After that, the PLL functionalized fiber was incubated for 1 h at room temperature in a 0.75 μM TBA solution, and then washed again with the Tris solution for 5 min by immersion. Finally, THR detection was performed by immersion of the optical fiber into THR solutions with concentrations from 0.01 to 100 nM for 30 min. The THR solution was prepared on a Tris-HCl buffer affinity solution composed of 0.39 g of Tris-base, 0.73 g of NaCl, 0.051 g of $\text{MgCl}_2 \cdot \text{H}_2\text{O}$, and dropwise addition of HCl 1 M to adjust the solution pH to 7.4 for a final volume of 50 mL. All the spectra were measured at the final time of each incubation step and washed three times with the Tris solution.

The cross-reactivity test with HTR was conducted by preparing the fiber as before and functionalizing the immobilized Au NPs with PLL and TBA resulting in a plasmonic band located at 592 nm. Then, after a 30 min incubation with HTR (140 nM in Tris-HCl buffer affinity solution), the spectra were measured, and the fiber was washed with the Tris solution.

Numerical analysis. All data analysis treatments and simulations were done in Python. The experimental plasmonic band curves were all smooth using a Savitzky-Golay filter. The maximum plasmonic bands were all obtained by fitting a Gaussian curve on a wavelength span of 100 nm centered around the peak and retrieving the fitting parameters. The RIS values at different RI regions were calculated by fitting wavelengths corresponding to the maximum plasmonic band position with respect to the external medium RI by second-order polynomial curves. After, their slope was calculated in specific regions retrieving the RIS values shown.

The determination of the NP diameter and fiber surface coverage was performed by analyzing the SEM images with

the ImageJ software. The NP diameter was calculated using 100 measurements and the surface coverage density with 25 measurements of multiple images across different areas of the fiber sensor region. The standard deviation and mean values were determined using a normal distribution fitting.

Simulations. The light-guiding profile of the multimode optical fibers was simulated using a paraxial approach with an angular distribution from real data [73] and corrected by an interaction factor given by $N = L/(D \tan \theta)$, where L is the sensor length and D is the fiber diameter. The final interaction is then obtained from the integration of all angular contributions. The fiber and the surrounding medium were modeled as infinite layers, made of glass and a constant RI ($n = 1.333 + \Delta n$), respectively, where Δn is used to test for bulk RI sensitivity. The simulations with multiple NPs were made using a Python library based on both the T-matrix and scattering-matrix for the interparticle and particle-layer interactions [54]. The non-intersecting NPs were placed sequentially and randomly over an area of $1 \mu\text{m}^2$ on the glass layer until the desired particle density was achieved. The integrated extinction cross sections were evaluated in reflection mode at angles that suffice the required light guiding conditions for the $600 \mu\text{m}$ multimode fiber. The simulations using the GEMA were made using the angular integrated reflectivity within a TMM framework [62]. The light was p-polarized and launched from the infinite glass layer. Glass and gold materials used in the simulations were taken from real data measurements, respectively, in Refs. [74,75].

APPENDIX B: CALCULATED EFFECTIVE INDEX AND OPTICAL RESPONSE

Calculated effective index through the Maxwell-Garnett effective index approximation for distinct Au densities is shown in Fig. 8. Figure 9 exhibits the calculated optical response from

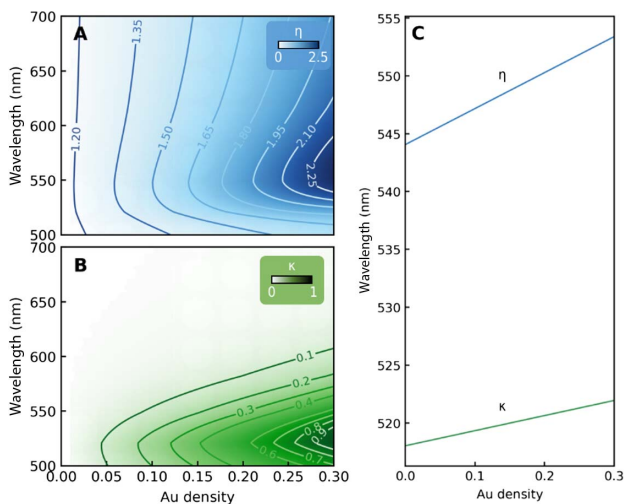


Fig. 8. Calculated effective index through the Maxwell-Garnett effective index approximation for distinct Au densities. The complex material refractive index is shown for its real (A) and imaginary (B) components. C: Wavelength of the effective index maxima for the Au densities ranging between 0 and 0.3.

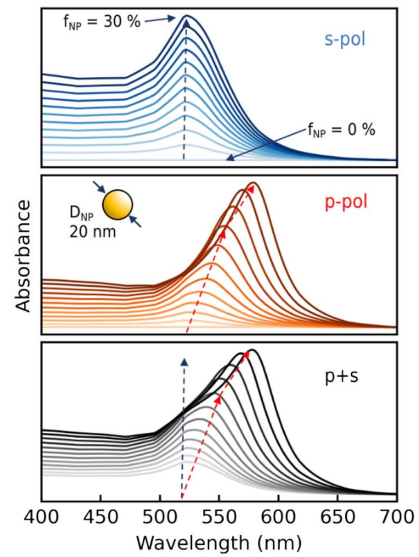


Fig. 9. Calculated optical response from the GEMA structure for a 20 nm layer under s-polarization, p-polarization, and the sum of both (p + s) for increasing f_{NP} from 0 to 30% in steps of 2.5% (represented from the lighter to the darker curves).

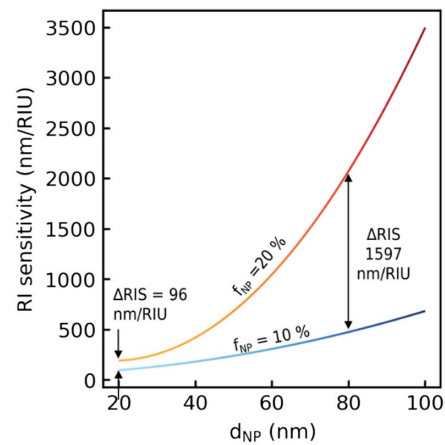


Fig. 10. Comparison of the RI sensitivity at f_{NP} of 10% (blue curve) and 20% (red curve) as calculated through the GEMA for NP diameters between 20 and 100 nm. The RI sensitivity difference (ΔRIS) between both curves is shown for NP diameters of 20 and 80 nm.

the GEMA structure for a 20 nm layer. In addition, RI sensitivity at f_{NP} of 10% and 20% is compared, as shown in Fig. 10.

Funding. Fundação para a Ciência e a Tecnologia (CEECIND/00471/2017, Grant Agreement 101084383, SFRH/BD/130674/2017, SFRH/BD/146784/2019); Xunta de Galicia (GRC ED431C 2020/09).

Disclosures. The authors declare no conflicts of interest.

Data Availability. Data underlying the results presented in this paper are not publicly available at this time but may be obtained from the authors upon reasonable request.

REFERENCES

- A. K. Sharma, A. Kumar Pandey, and B. Kaur, "A review of advancements (2007–2017) in plasmonics-based optical fiber sensors," *Opt. Fiber Technol.* **43**, 20–34 (2018).
- M. Bauch, K. Toma, M. Toma, *et al.*, "Plasmon-enhanced fluorescence biosensors: a review," *Plasmonics* **9**, 781–799 (2014).
- C. L. Wong and M. Olivo, "Surface plasmon resonance imaging sensors: a review," *Plasmonics* **9**, 809–824 (2014).
- H. Malekzad, P. S. Zangabad, H. Mirshekari, *et al.*, "Noble metal nanoparticles in biosensors: recent studies and applications," *Nanotechnol. Rev.* **6**, 301–329 (2018).
- H. Lu, Z. Tian, H. Yu, *et al.*, "Optical fiber with nanostructured cladding of TiO₂ nanoparticles self-assembled onto a side polished fiber and its temperature sensing," *Opt. Express* **22**, 32502–32508 (2014).
- P. Sharma, V. Semwal, and B. D. Gupta, "Highly sensitive and selective localized surface plasmon resonance biosensor for detecting glutamate realized on optical fiber substrate using gold nanoparticles," *Photonics Nanostruct.* **37**, 100730 (2019).
- H. Manoharan, D. Kc, and V. V. R. Sai, "Controlled *in situ* seed-mediated growth of gold and silver nanoparticles on an optical fiber platform for plasmonic sensing applications," *Plasmonics* **15**, 51–60 (2020).
- H. M. Kim, D. H. Jeong, H. Y. Lee, *et al.*, "Improved stability of gold nanoparticles on the optical fiber and their application to refractive index sensor based on localized surface plasmon resonance," *Opt. Laser Technol.* **114**, 171–178 (2019).
- B. T. Wang and Q. Wang, "Sensitivity-enhanced optical fiber biosensor based on coupling effect between SPR and LSPR," *IEEE Sens. J.* **18**, 8303–8310 (2018).
- P. S. S. Dos Santos, J. P. Mendes, B. Dias, *et al.*, "Spectral analysis methods for improved resolution and sensitivity: enhancing SPR and LSPR optical fiber sensing," *Sensors* **23**, 1666 (2023).
- L. P. F. Peixoto, J. F. L. Santos, and G. F. S. Andrade, "Plasmonic nanobiosensor based on Au nanorods with improved sensitivity: a comparative study for two different configurations," *Anal. Chim. Acta* **1084**, 71–77 (2019).
- L. Guo, J. A. Jackman, H. H. Yang, *et al.*, "Strategies for enhancing the sensitivity of plasmonic nanosensors," *Nano Today* **10**, 213–239 (2015).
- E. Martinsson, B. Sepulveda, P. Chen, *et al.*, "Optimizing the refractive index sensitivity of plasmonically coupled gold nanoparticles," *Plasmonics* **9**, 773–780 (2014).
- Q. Wu, Y. Semenova, P. Wang, *et al.*, "High sensitivity SMS fiber structure based refractometer—analysis and experiment," *Opt. Express* **19**, 7937–7944 (2011).
- F. Han, T. Lang, B. Mao, *et al.*, "Surface plasmon resonance sensor based on coreless fiber for high sensitivity," *Opt. Fiber Technol.* **50**, 172–176 (2019).
- S. Jia, C. Bian, J. Sun, *et al.*, "Gold nanospheres-coated LSPR fiber sensor with high RI sensitivity by a rapid fabricating method," in *NEMS 2018—13th Annual IEEE International Conference on Nano/Micro Engineered and Molecular Systems* (2018), pp. 523–526.
- P. Nordlander, C. Oubre, E. Prodan, *et al.*, "Plasmon hybridization in nanoparticle dimers," *Nano Lett.* **4**, 899–903 (2004).
- M. A. Basyooni, A. M. Ahmed, and M. Shaban, "Plasmonic hybridization between two metallic nanorods," *Optik-Stuttgart* **172**, 1069–1078 (2018).
- E. Prodan, C. Radloff, N. J. Halas, *et al.*, "A hybridization model for the plasmon response of complex nanostructures," *Science* **302**, 419–422 (2003).
- H. Zhang, J. Cadusch, C. Kinnear, *et al.*, "Direct assembly of large area nanoparticle arrays," *ACS Nano* **12**, 7529–7537 (2018).
- M. Sturaro, G. Zacco, P. Zilio, *et al.*, "Gold nanodisks plasmonic array for hydrogen sensing at low temperature," *Sensors* **19**, 3–9 (2019).
- M. Toma, K. Cho, J. B. Wood, *et al.*, "Gold nanoring arrays for near infrared plasmonic biosensing," *Plasmonics* **9**, 765–772 (2014).
- J. Jiang, X. Wang, S. Li, *et al.*, "Plasmonic nano-arrays for ultrasensitive bio-sensing," *Nanophotonics* **7**, 1517–1531 (2018).
- S. Q. Li, P. Guo, L. Zhang, *et al.*, "Infrared plasmonics with indium tin-oxide nanorod arrays," *ACS Nano* **5**, 9161–9170 (2011).
- N. Malikova, I. Pastoriza-Santos, M. Schierhorn, *et al.*, "Layer-by-layer assembled mixed spherical and planar gold nanoparticles: control of interparticle interactions," *Langmuir* **18**, 3694–3697 (2002).
- S. K. Ghosh and T. Pal, "Interparticle coupling effect on the surface plasmon resonance of gold nanoparticles: from theory to applications," *Chem. Rev.* **107**, 4797–4862 (2007).
- C. Fernández-López, M.-M. Cintia, A. Alvarez-Puebla, *et al.*, "Highly controlled silica coating of peg-capped metal nanoparticles and preparation of SERS-encoded particles," *Langmuir* **25**, 13894–13899 (2009).
- R. P. M. Höller, C. Kuttner, M. Mayer, *et al.*, "Colloidal superstructures with triangular cores: size effects on SERS efficiency," *ACS Photonics* **7**, 1839–1848 (2020).
- E. C. Le Ru and P. G. Etchegoin, "Sub-wavelength localization of hot-spots in SERS," *Chem. Phys. Lett.* **396**, 393–397 (2004).
- A. B. Evlyukhin and S. I. Bozhevolnyi, "Surface plasmon polariton guiding by chains of nanoparticles," *Laser Phys. Lett.* **3**, 396–400 (2006).
- P. J. Compajien, V. A. Malyshev, and J. Knoester, "Engineering plasmon dispersion relations: hybrid nanoparticle chain-substrate plasmon polaritons," *Opt. Express* **23**, 2280–2292 (2015).
- M. M. Miller and A. A. Lazarides, "Sensitivity of metal nanoparticle plasmon resonance band position to the dielectric environment as observed in scattering," *J. Opt. A* **8**, 21556–21565 (2006).
- N. Hounghamhang, S. Charoensuwan, O. Sonthipakdee, *et al.*, "Gold-nanoparticle-based fiber optic sensor for sensing the refractive index of environmental solutions," *Chiang Mai J. Sci.* **45**, 2168–2177 (2018).
- X. Zhong, L. Ma, G. Yin, *et al.*, "Hg²⁺ optical fiber sensor based on LSPR with PDDA-templated AuNPs and CS/PAA Bilayers," *Appl. Sci.* **10**, 4845 (2020).
- M. A. Otte, M. C. Estévez, D. Regatos, *et al.*, "Guiding light in monolayers of sparse and random plasmonic meta-atoms," *ACS Nano* **5**, 9179–9186 (2011).
- H. Chen, X. Kou, Z. Yang, *et al.*, "Shape- and size-dependent refractive index sensitivity of gold nanoparticles," *Langmuir* **24**, 5233–5237 (2008).
- S. Jia, C. Bian, J. Sun, *et al.*, "A wavelength-modulated localized surface plasmon resonance (LSPR) optical fiber sensor for sensitive detection of mercury(II) ion by gold nanoparticles-DNA conjugates," *Biosens. Bioelectron.* **114**, 15–21 (2018).
- W. Te Wu, C. H. Chen, C. Y. Chiang, *et al.*, "Effect of surface coverage of gold nanoparticles on the refractive index sensitivity in fiber-optic nanoplasmonic sensing," *Sensors* **18**, 1759 (2018).
- J. A. García, D. Monzón-Hernández, J. Manríquez, *et al.*, "One step method to attach gold nanoparticles onto the surface of an optical fiber used for refractive index sensing," *Opt. Mater.-Amsterdam* **51**, 208–212 (2016).
- M. Lin, M. Lu, Y. Liang, *et al.*, "Polyelectrolyte-enhanced localized surface plasmon resonance optical fiber sensors: properties interrogation and bioapplication," *ACS Appl. Nano Mater.* **5**, 6171–6180 (2022).
- M. H. Tu, T. Sun, and K. T. V. Grattan, "Optimization of gold-nanoparticle-based optical fibre surface plasmon resonance (SPR)-based sensors," *Sens. Actuators B Chem.* **164**, 43–53 (2012).
- E. Martinsson, M. A. Otte, M. M. Shahjamali, *et al.*, "Substrate effect on the refractive index sensitivity of silver nanoparticles," *J. Phys. Chem. C* **118**, 24680–24687 (2014).
- S. M. Marinakos, S. Chen, and A. Chilkoti, "Plasmonic detection of a model analyte in serum by a gold nanorod sensor," *Anal. Chem.* **79**, 5278–5283 (2007).
- Y. Khalavka, J. Becker, and C. Sönnichsen, "Synthesis of rod-shaped gold nanorattles with improved plasmon sensitivity and catalytic activity," *J. Am. Chem. Soc.* **131**, 1871–1875 (2009).

45. R. Chikkaraddy and J. J. Baumberg, "Accessing plasmonic hotspots using nanoparticle-on-foil constructs," *ACS Photonics* **8**, 2811–2817 (2021).
46. H. Sugimoto, S. Yashima, and M. Fujii, "Hybridized plasmonic gap mode of gold nanorod on mirror nanoantenna for spectrally tailored fluorescence enhancement," *ACS Photonics* **5**, 3421–3427 (2018).
47. L. Liu, A. V. Krasavin, J. Zheng, *et al.*, "Atomically smooth single-crystalline platform for low-loss plasmonic nanocavities," *Nano Lett.* **22**, 1786–1794 (2022).
48. A. Urrutia, J. Goicoechea, and F. J. Arregui, "Optical fiber sensors based on nanoparticle-embedded coatings," *J. Sens.* **2015**, 805053 (2015).
49. Q. Wang, X. Yin, P. Yin, *et al.*, "Research progress of resonance optical fiber sensors modified by low-dimensional materials," *Laser Photonics Rev.* **17**, 2200859 (2023).
50. H. Wang, "Plasmonic refractive index sensing using strongly coupled metal nanoantennas: nonlocal limitations," *Sci. Rep.* **8**, 9589 (2018).
51. B. Špačková, M. L. Ermini, and J. Homola, "High-performance biosensor exploiting a light guidance in sparse arrays of metal nanoparticles," *Opt. Lett.* **44**, 1568–1571 (2019).
52. V. A. Markel, "Introduction to the Maxwell Garnett approximation: tutorial," *J. Opt. Soc. Am. A* **33**, 1244–1256 (2016).
53. U. Hohenester and A. Trügler, "MNPBEM—a MATLAB toolbox for the simulation of plasmonic nanoparticles," *Comput. Phys. Commun.* **183**, 370–381 (2012).
54. A. Egel, K. M. Czajkowski, D. Theobald, *et al.*, "SMUTHI: a Python package for the simulation of light scattering by multiple particles near or between planar interfaces," Accessed on 28 July 2022 [Online]. Available: <https://smuthi.readthedocs.io>.
55. M. S. Maurice, N. Barros, and H. Kachkachi, "Beyond the Maxwell Garnett approximation for interacting plasmonic nanoparticles: an analytical and numerical study," *J. Appl. Phys.* **134**, 094303 (2023).
56. W. Park, "Optical interactions in plasmonic nanostructures," *Nano Converg.* **1**, 2 (2014).
57. D. Sun, L.-P. Sun, T. Guo, *et al.*, "Label-free thrombin detection using a tapered fiber-optic interferometric aptasensor," *J. Lightwave Technol.* **37**, 2756–2761 (2019).
58. L. Coelho, J. M. M. de Almeida, J. L. Santos, *et al.*, "Aptamer-based fiber sensor for thrombin detection," *J. Biomed. Opt.* **21**, 087005 (2016).
59. N. Cennamo, L. Pasquardini, F. Arcadio, *et al.*, "D-shaped plastic optical fibre aptasensor for fast thrombin detection in nanomolar range," *Sci. Rep.* **9**, 18740 (2019).
60. T. Ayupova, M. Shaimerdenova, M. Sypabekova, *et al.*, "Picomolar detection of thrombin with fiber-optic ball resonator sensor using optical backscatter reflectometry," *Optik-Stuttgart* **241**, 166969 (2021).
61. J. Lao, L. Han, Z. Wu, *et al.*, "Gold nanoparticle-functionalized surface plasmon resonance optical fiber biosensor: *in situ* detection of thrombin with 1 nm detection limit," *J. Lightwave Technol.* **37**, 2748–2755 (2019).
62. K. M. Czajkowski, D. Świtlik, C. Langhammer, *et al.*, "Effective optical properties of inhomogeneously distributed nanoobjects in strong field gradients of nanoplasmonic sensors," *Plasmonics* **13**, 2423–2434 (2018).
63. R. Ruppini, "Evaluation of extended Maxwell-Garnett theories," *Opt. Commun.* **182**, 273–279 (2000).
64. E. Klantsataya, A. François, H. Eberndorf-Heidepriem, *et al.*, "Surface plasmon scattering in exposed core optical fiber for enhanced resolution refractive index sensing," *Sensors* **15**, 25090–25102 (2015).
65. M. C. Navarrete, N. Díaz-Herrera, A. González-Cano, *et al.*, "A polarization-independent SPR fiber sensor," *Plasmonics* **5**, 7–12 (2010).
66. Y. Zhao, Z.-Q. Deng, and Q. Wang, "Fiber optic SPR sensor for liquid concentration measurement," *Sens. Actuators B Chem.* **192**, 229–233 (2014).
67. H. S. Jang, K. N. Park, C. D. Kang, *et al.*, "Optical fiber SPR biosensor with sandwich assay for the detection of prostate specific antigen," *Opt. Commun.* **282**, 2827–2830 (2009).
68. S. Enoch and N. Bonod, *Plasmonics—From Basics to Advanced Topics* (Springer, 2012), p. 167.
69. C. M. Danforth, T. Orfeo, S. J. Everse, *et al.*, "Defining the boundaries of normal thrombin generation: investigations into hemostasis," *PLoS ONE* **7**, e30385 (2012).
70. S. D. Weaver and R. J. Whelan, "Characterization of DNA aptamer–protein binding using fluorescence anisotropy assays in low-volume, high-efficiency plates," *Anal. Methods* **13**, 1302–1307 (2021).
71. S. Goutelle, M. Maurin, F. Rougier, *et al.*, "The Hill equation: a review of its capabilities in pharmacological modelling," *Fundam. Clin. Pharmacol.* **22**, 633–648 (2008).
72. N. G. Bastús, J. Comenge, and V. Puntès, "Kinetically controlled seeded growth synthesis of citrate-stabilized gold nanoparticles up to 200 nm: size focusing versus Ostwald ripening," *Langmuir* **27**, 11098–11105 (2011).
73. M. Yasukawa, O. Sugihara, and S. Kobayashi, "Launch light dependency of step-index multimode fiber connections analyzed by modal power distribution using encircled angular flux," *Appl. Opt.* **56**, 876–883 (2017).
74. P. B. Johnson and R. W. Christy, "Optical constants of the noble metals," *Phys. Rev. B* **6**, 4370 (1972).
75. I. H. Malitson, "Interspecimen comparison of the refractive index of fused silica," *J. Opt. Soc. Am.* **55**, 1205–1209 (1965).